

Xun Yao,¹ Ming Yao,¹ and Bugao Xu¹

Automated Measurements of Road Cracks Using Line-Scan Imaging

ABSTRACT: This paper presents a new line-scan imaging system for automated measurements of road crack. The system consists of off-the-shelf hardware for real-time image acquisition and the customized image-analysis software for crack detection. A line-scan camera with 2 k pixels, a GigE interface, and a line rate up to 36 kHz was used to scan 3.6-m wide pavements at highway speeds, and a laser line projector was used to cast a transverse beam that overlays the scanline of the camera to eliminate shadows of vehicles and roadside objects and to maintain consistent lighting conditions. In the crack detection algorithms, a pavement image was first divided into grids of 8×8 pixels, and each grid was classified either as a non-crack or crack grid (called seed) using the pixel information of the grid and the overall background. Then, seeds in the vicinity were connected based on geometrical and intensity constraints. The connected seeds served as a candidate for a crack, which were further verified by using the contrast to the pixels along its trace. The paper also reports the experimental results on a designated pavement that was manually rated by an expert, and scanned three-times by the system. The statistic analysis showed that the difference in crack length between the manual and automatic measurements was less than 10 %, and no significant difference among the multiple scans by the system.

KEYWORDS: line-scan imaging, crack detection, pavement inspection

Introduction

Information about the type, severity, and extent of surface distress is essential for assessing the pavement conditions. Cracking is the most common form of distress which undermines the pavement's integrity and long-term performance. Intelligent pavement maintenance decisions rely on regular and reliable inspection of cracking and other forms of distress. From the early 1970s, researchers have striven to develop various automated pavement distress survey (APDS) systems to replace visual rating methods in order to reduce traffic disturbance, survey cost and risk to human inspectors, and to provide more objective and prompt results for rehabilitation management [1–6]. Most APDS systems have one or more cameras installed on a moving vehicle to capture dynamic pavement images, and then extract cracks (as narrow as 1 mm) from the images in either a real-time or an offline process. Given the complexity of pavement textures and lighting conditions, implementing such a system presents many challenges. By now, no APDS system has been truly able to perform real-time, highway-speed, full-lane, whole-distance surveys with repeatable and accurate data.

APDS systems differ in their image acquisition devices. These devices include video, area-scan, and line-scan cameras. Recent advancements in charged-coupled device and complementary metal-oxide-semiconductor sensor technology dramatically increases camera's resolution, sensitivity, and frame/line rate, making line-scan cameras particularly suitable for pavement inspection. A line-scan camera with 2 k pixels, a GigE interface, and a line rate up to 36 kHz has greatly enabled a system to meet the need for fast, reliable, and high-resolution image acquisition.

APDS systems also differ in their lighting approaches. In the earlier stage, some systems were designed to use natural light for its simplicity and vehicular energy conservation. Obviously, shadows

of vehicles and roadside objects in an image cause many problems in crack detection. As a result, current APDS systems require special lighting devices to illuminate pavements to prevent shadows from the image and to maintain consistent imaging conditions.

To work with a line-scan camera, a lighting device normally needs to cast a transverse beam to overlay the camera line that usually covers one full lane (3.6 m wide). Halogen or florescent lamps [7–10], light-emitting diode (LED) arrays [11], and laser line projectors [12,13] are three common light sources used in APDS systems. Halogen or florescent lamps generate white lights which can only alleviate shadows to a limited extent because no camera filters can be used to block the sunlight. Light assemblies with multiple halogen or florescent lamps require a devoted power generator due to high power consumption. The assemblies often have dimensions wider than the vehicle body, thus increasing accident risks particularly when driving in urban areas.

We designed an LED light bar for an APDS system used by the Texas Department of Transportation (TxDOT) [11]. The light bar used 400 ultra bright red LEDs and a cylindrical lens to form a linear beam of approximately 25 mm (W) \times 3050 mm (L) on the pavement. A band-pass filter that matches the wavelength of the red LED was used to reduce the sunlight and thus to gain almost shadow-free images. However, the light bar can only project a focused beam at a 0.3 m distance from the ground, and it is 0.6 m wider than the vehicle body. In addition, those high-power LEDs lose efficiency quickly when overheated, making the survey operation much more difficult in summer time.

Recently, laser line projection has become a dominant means for illuminating a line-scan camera in APDS systems because of its high efficiency and compact size. A laser projector is an off-the-shelf product that is easy to install and maintain. It can reduce the on-vehicle energy consumption from several kilowatts of incandescent lighting or several hundred watts in LED lighting to around 70 W. It is also easy to provide adequate cooling through the vehicle air-conditioning system to the laser projector so that it can function more reliably in outdoor environments. This paper is to report the new development of a system, called Crackscope [14], using a laser

Manuscript received August 25, 2010; accepted for publication January 10, 2011; published online February 2011.

¹Center for Transportation Research, Univ. of Texas at Austin, Austin, TX 78712.



FIG. 1—Crackscope on the vehicle.

line projector and a line-scan camera to acquire pavement images for crack detections, and the experimental results of its accuracy and repeatability tests.

System Configuration

The Crackscope uses a Dalsa 2 k line-scan camera (referred to as camera) and a StockerYale Magnum II line projector (referred to as projector) to scan a 3.6-m wide lane as the survey vehicle moves forward. The projector has an 810 nm 4 w laser diode to illuminate the pavement, and the camera has a band-pass filter, whose peak transmittance is at 800 nm, to eliminate shadows of the vehicle and roadside objects. The camera utilizes a GigE interface to connect to the computer, and its line scan rate, exposure time, gain, and other parameters can be dynamically adjusted. The projector and camera are mounted side by side inside an enclosure, and aligned to ensure the laser line to overlap entirely with the camera’s scanline. The enclosure is installed vertically downward on the survey vehicle at a height of 2.3 m above the ground (see Fig. 1).

Figure 2 shows the mounting geometry of the Crackscope. The camera has a view angle of 77° that covers a 3.6 m wide pavement, giving a ground resolution of 1.76 mm/pixel. The camera captures a line image at a time and sends individual lines to the computer’s

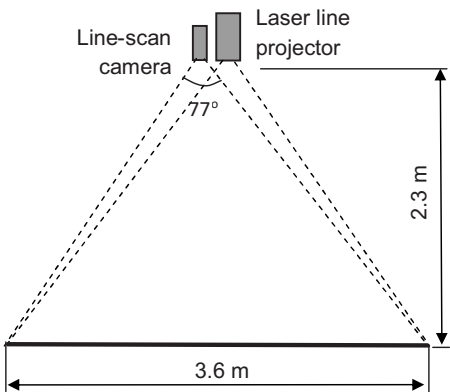


FIG. 2—Mounting geometry.

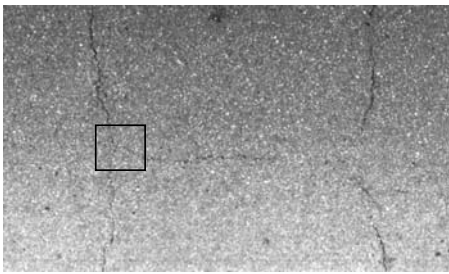


FIG. 3—Sample image.

buffer through the GigE cable to form one frame of image when a certain number of lines are accumulated. The cumulative lines per image can be set from 1024 to 6144 (1.8 to 10.8 m in distance). The line scan rate of the camera is calculated based on the vehicle speed, which is obtained from the GPS, and modified instantaneously to ensure that each line covers approximately the same distance on the pavement when the travelling speed varies. The exposure time of the image sensor is also controlled dynamically to prevent the image from being over- or under-exposed. Due to the nature of the non-uniform power distribution across the laser beam, the image may contain longitudinal streaks that are difficult to be differentiated from real cracks. This non-uniformity in the image can be literally removed by resetting the camera’s coefficients on a pixel-by-pixel basis in reference to a white target placed underneath the camera and the projector. Figure 3 gives one example of pavement images taken by the Crackscope.

Since the high power infrared laser projector (class IIIB) is potentially hazardous to the unprotected human eyes, strict safety measures must be implemented to meet operation requirements mandated in many states in the United States. In addition to two manually operated switches (S_1 and S_2 in Fig. 4) to control the power and the safety interlock of the projector, one proximity sensor is mounted on the front plate of the enclosure to detect any object in a 1.5 m range and to regulates a relay (S_3 in Fig. 4) that can turn on/off the safety interlock. The GPS unit sends the vehicle speed to the computer at a rate of at least three times per second. Whenever the speed is below a given speed, e.g., 5 km/h, the computer sends a signal to a digital input/output board, whose output is connected to the modulation port of the projector, and the output power of the laser is cut off instantaneously. The proximity sensor and the speed modulation provide dual protections to a nearby person when the vehicle is stationary or in slow motion.

Crack Detection Algorithms

In the past several decades, many crack detection methods have been developed in various automated pavement inspection systems [15–17]. In general, these methods can be classified into two major

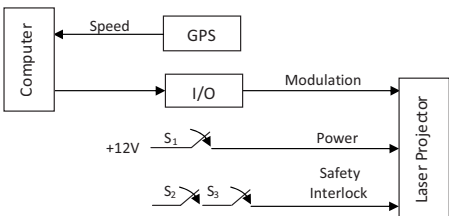


FIG. 4—Safety controls (S_1 : Keylock switch; S_2 : Switch; S_3 : Relay).

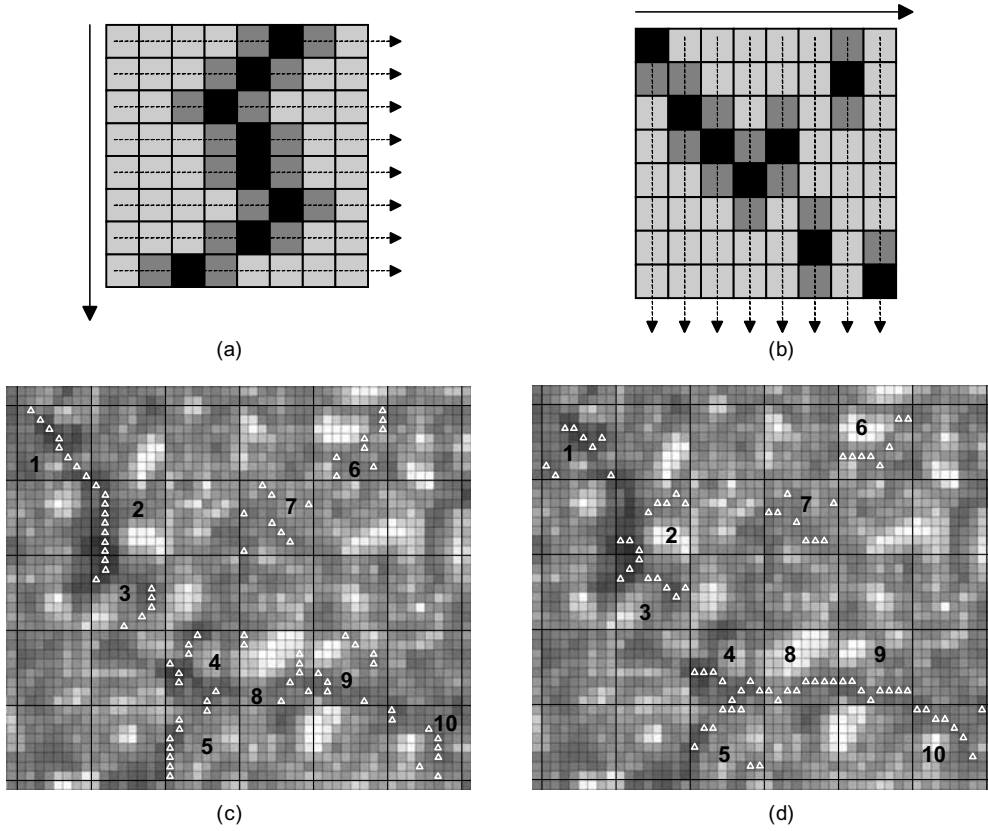


FIG. 5—Grid feature computation.

categories: Thresholding methods [18–20] and edge-detection methods [21,22]. Because most of these methods are based on local crack information only, the detection accuracy varies greatly with image quality and background features [15].

A primary clue for detecting cracks in a pavement image is that a crack consists of a narrow strip of pixels whose intensities are appreciably darker or whiter than the surrounding background. But, a crack strip is often interrupted by surface gravels, or filled with dirt, and thus has various widths and intensities along its pass. Skid marks, oil spills and many other non-crack textures may have features similar to cracks, adding ambiguity to crack detection. A commonly used strategy for crack detection is to first locate all possible crack pixels based on localized features (the locating process), and then to trace marked pixels using geometrical and intensity constraints (the tracing process). This strategy often has high false detection rates because only the local features are used [23]. We propose a new crack-detection algorithm by adding the features of neighboring background regions to local feature detection, and then verifying cracks with geometrical and intensity constraints in the tracing process. To begin, the original image is divided into a set of $n \times n$ sub-regions, which are referred to as “grids.” The grid size should be small enough to allow only one crack to pass through but large enough to contain enough surrounding pixels. For the images captured by our system (1.76 mm/pixel), 8×8 pixels are a typical size for the grid.

Grid Feature Extraction

Since a crack is directional, we use vertical and horizontal features to characterize a grid. Figure 5 shows a grid in which the darkest

pixel is being searched row by row to locate a vertical feature line Fig. 5(a), and column by column to locate a horizontal feature line Fig. 5(b). Along the vertical feature line, a one-dimensional convolution can be applied to each pixel. After denoting the intensity of a pixel at (i, j) as $I(i, j)$ and the size of the grid as (m, n) and the grid top left pixel coordinate as (x_0, y_0) , the vertical feature F_v can be computed as

$$F_v = \frac{1}{n} \sum_{j=0}^{n-1} \min_{i=0}^{m-1} \left\{ \sum_{k=0}^{l-1} w_k [I(x_0 + i + k, y_0 + j) + I(x_0 + i - k, y_0 + j)] \right\} \quad (1)$$

where:

l = width of the convolution template, and
 w_k = sample weights of a normal distribution.

By choosing different l and w_k , we can target cracks of different widths. F_v is the mean intensity of a group of the selected darker pixels. For computational convenience, w_k can be normalized as $2w_0 + \sum_{k=1}^{l-1} w_k = 1$. When $w_k|_{k \neq 0} = 0$, F_v is degraded to the mean intensity of the m darkest pixels. Meanwhile, the variance v_v^2 of the selected minimum pixels can be calculated as

$$v_v^2 = \frac{1}{n} \sum_{j=0}^{n-1} \left(\min_{i=0}^{m-1} \left\{ \sum_{k=0}^{l-1} w_k [I(x_0 + i + k, y_0 + j) + I(x_0 + i - k, y_0 + j)] \right\} - F_v \right)^2 \quad (2)$$

Similarly, the horizontal features—mean intensity F_h and variance

v_v^2 —can be calculated based on the horizontal feature line as follows:

$$F_h = \frac{1}{m} \sum_{i=0}^{m-1} \min_{j=0}^{n-1} \left\{ \sum_{k=0}^{l-1} w_k [I(x_0 + i, y_0 + j + k) + I(x_0 + i, y_0 + j - k)] \right\} \quad (3)$$

$$v_h^2 = \frac{1}{m} \sum_{i=0}^{m-1} \left(\min_{j=0}^{n-1} \left\{ \sum_{k=0}^{l-1} w_k [I(x_0 + i, y_0 + j + k) + I(x_0 + i, y_0 + j - k)] \right\} - F_h \right)^2 \quad (4)$$

Figure 5(c) and 5(d) are the amplified views of a pavement region marked by a rectangle in Fig. 3, illustrating different types of grids in different searching directions. Figure 5(c) shows the vertical searching and Fig. 5(d) shows the horizontal searching. In the two figures, a small square indicates the single pixel and a large square (8×8 pixels) is the selected grid. The small triangles represent the searched pixels. Grids 2, 3, and 5 demonstrate the typical vertical crack grids. Grids 4, 8, and 9 indicate the typical horizontal vertical crack grids. Grids 6 and 7 demonstrate the typical background grids. Grids 1 and 10 show two diagonal crack grids. These searched grids have potential to be counted as crack seeds, which need to be further identified in the following process.

Seed Identification

The vertical and horizontal features of a grid can be used to identify the grid as a “seed” or background grid. Considering that the grid feature is a random variable, background pixel gray level η and seed feature ξ have normal distribution: $\xi \sim N(\mu_s, \sigma_s)$ and $\eta \sim N(\mu_b, \sigma_b)$. Then, the seed identification problem becomes a hypothesis test

$$\begin{aligned} H_0: \mu_s &\geq \mu_b \\ H_1: \mu_s &< \mu_b \end{aligned} \quad (5)$$

A statistic u can be constructed, and it subjects to a standard normal distribution

$$u = (\bar{\eta} - \bar{\xi}) / \sqrt{\sigma_s^2/n_1 + \sigma_b^2/n_2} \sim N(0, 1) \quad (6)$$

Thus, we get the test as

$$\begin{aligned} &H_0 \\ &u < k_\alpha \\ &H_1 \end{aligned} \quad (7)$$

where:

$\int_{-\infty}^{k_\alpha} \frac{1}{\sqrt{2\pi}} \exp(-(v^2/2)) dv = 1 - \alpha$ (α is the level of significance),

$\bar{\xi}$ = sample mean of a seed feature, and

$\bar{\eta}$ = sample mean of a background region gray level.

This hypothesis test provides a basis to separate a seed grid from the background.

In practice, $\bar{\eta}$ and σ_b can be calculated with the pixel gray level mean and variance of the large background near the grid, and $\bar{\xi}$ and σ_s are calculated with the mean and variance of the current grid

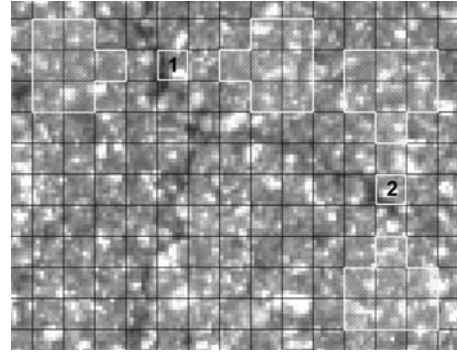


FIG. 6—Seed grid identification.

features, either (F_v, v_v) or (F_h, v_h) . $\sqrt{\sigma_s^2/n_1 + \sigma_b^2/n_2}$ can be approximated using a linear function, and Eq 1 can be further simplified to

$$|\bar{\eta} - \bar{\xi}| < k_s \cdot \sigma_s + k_b \cdot \sigma_b + k_c \quad (8)$$

where:

k_s, k_b, k_c = empirical values to adjust the weights of the background and the grid features in the threshold, and should be adaptive to various image characteristics.

Furthermore, $\bar{\eta}$ and σ_b can be calculated with the pixel gray level mean and variance of the background near the grid, and $\bar{\xi}$ and σ_s are calculated with the mean and variance of the current grid features. Figure 6 is the amplified view of the rectangular region marked in Fig. 3 that illustrates how to determine the background region. In the figure, the white single squares indicate the grids to be judged, and white shadowed regions located on two sides represent the background region for the corresponding grid. Two examples, grid 1 and grid 2 in Fig. 6(b), are given to illustrate the identification process in the horizontal and vertical directions, respectively.

Seed Connection

The seed identification process only took into account the localized features around a single grid. Many grids without real cracks can be identified as seeds. The seed connection is the tracing step to consider the relationship of a number of adjacent seeds with respect to the geometric and intensity constraints established for crack identification. The geometric constraints in defining a crack are relatively straightforward, which include the limits on minimal length, maximal width, and maximal change in orientation [23]. When seed grids are to be identified as potential crack seeds using the geometrical constraints, the pixels bridging these seeds need to be traced, and their homogeneity needs to be verified with intensity constraints for further confirmation.

For each seed grid, the darkest pixel (for black crack, and the brightest pixel for white crack) is defined as the centroid of the grid. Figure 7(a) shows two seed grids and their centroids C_1 and C_2 (two black squares). Stipulate that C_1 is the starting point and C_2 is the target point. Use the following steps to find bridging pixels between the two seeds:

- (1) Set C_1 as the current pixel C .
- (2) Compute the orientation O_p from C to C_2 .
- (3) Locate the darkest pixel d_0 within three pixels nearest to C along orientation O_p .

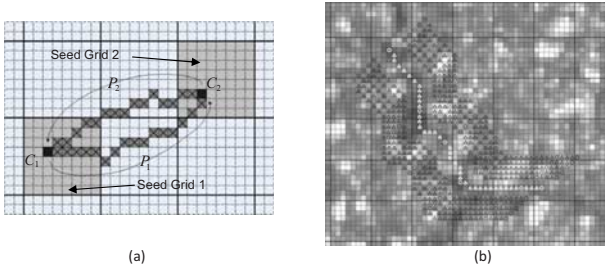


FIG. 7—(a) Tracing and (b) verifying seed grids.

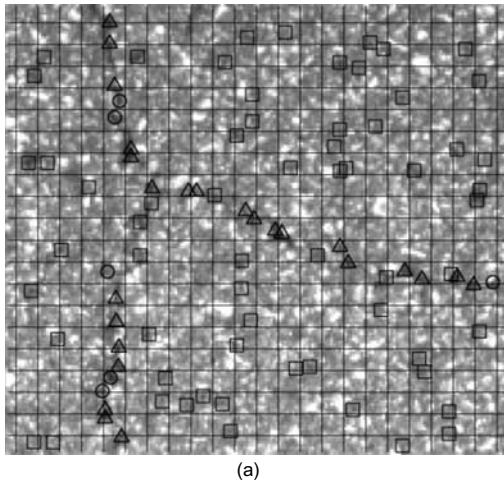
- (4) Store d_0 to connected set P_1 , and set it as the new current pixel C .
- (5) If the current pixel C is not C_2 , go to step (2). Otherwise, stop the tracing.

Exchange the starting point (C_2) and the end point (C_1), and repeat the tracing steps described above. Another point set P_2 will be obtained. Compare the means of the pixels in P_1 and P_2 , the pixel set with smaller mean will be selected, which is a candidate crack fragment between the two seed grids. Move the starting point to C_2 , and repeat the tracing process. If the tracing process eventually connects n grids, these n sets are the candidates for a crack that needs to be verified with intensity constraints.

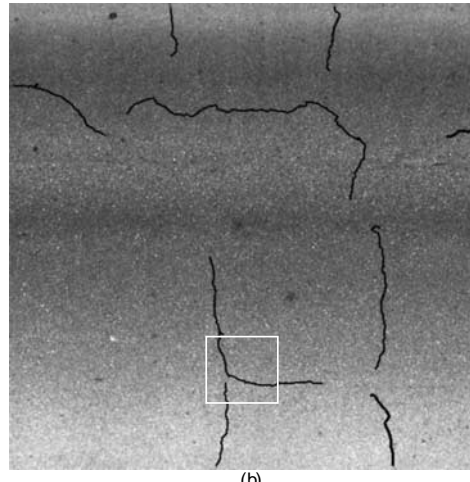
Denote the intensity mean and variance of the pixels in all selected sets as M_c and V_c . In principle, a crack should have darker and more coherent pixel clusters, that is, M_c and V_c should be discriminably lower than those (denoted as M_b and V_b) of a background region near the crack. Figure 7(b) gives an example of selecting the background pixels for a connected crack in a marked region in Fig. 3. The white small circles and triangles indicate the end and body pixels of a detected candidate crack, respectively. To verify if the candidate is a true crack, five parallel curves (black small circles and triangles) on both sides of the segment are chosen as the background for calculating M_b and V_b . Using a similar judgment method introduced in the section Seed Identification, we can get the following formula to identify the crack:

$$(M_b - M_c)^2 > w_c V_c / l + w_b V_b + w_0 \quad (9)$$

where:



(a)



(b)

FIG. 8—(a) Seed map and (b) detected cracks in a pavement image.

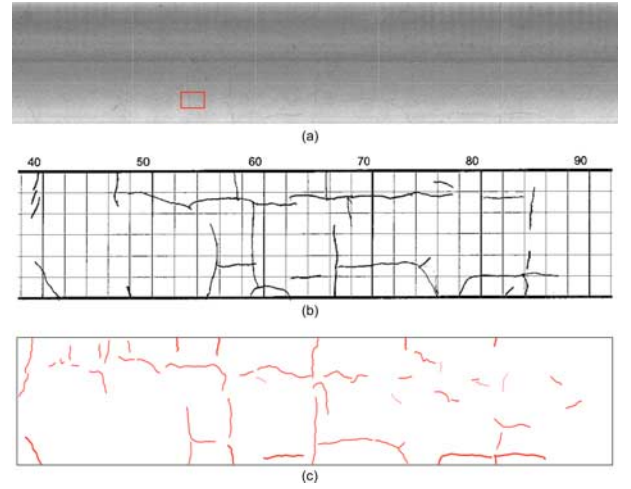


FIG. 9—(a) Stitched pavement images; (b) crack map by expert; and (c) crack map by Crackscope.

w_c , w_b , and w_0 =coefficients, which can be empirically determined using sample images, and l is the length of this candidate crack.

Figure 8(a) presents seeds map of the marked rectangle in Fig. 3. The black circles and triangles indicate the end and body grids of one connected crack cluster, respectively. The black squares represent the dispersed grids that unable to form a crack cluster with an enough length. Figure 8(b) shows a whole frame of a pavement image with resolution at 2048×2048 pixels, which contains the portion displayed in Fig. 3, and the rectangles in the two figures represent the same region. The detected cracks rendered with black curves. This frame is also one of the stitched images in Fig. 9(a), which were recorded in a validation test.

Validation Tests

To facilitate validation tests, the Crackscope measurements were compared with those obtained from the manual visual measurements of a 500-m long lane of a local asphalt street. The manual inspection was carried out by the experts of TxDOT. The automated

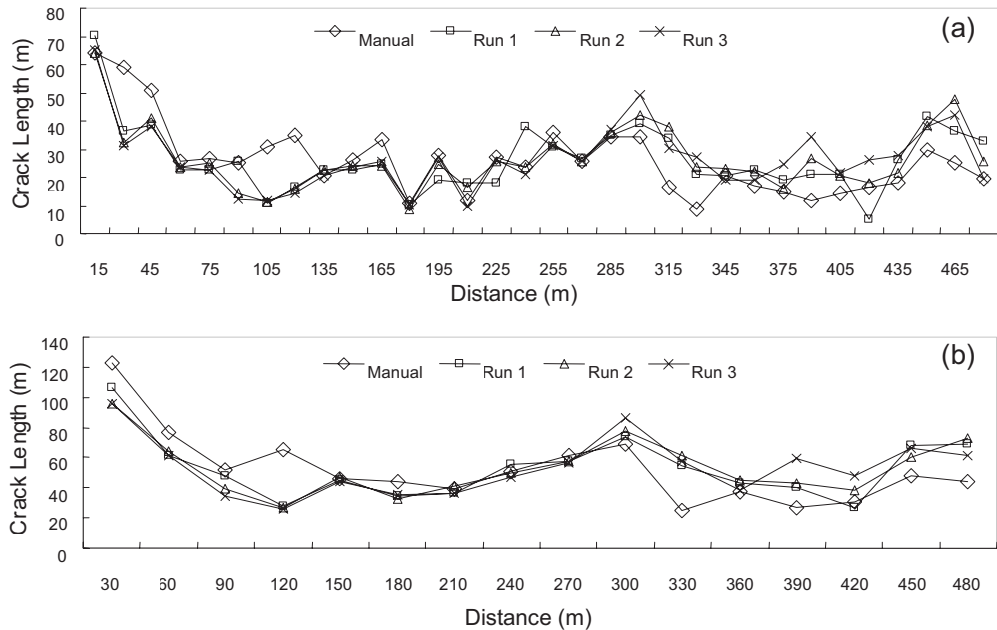


FIG. 10—Crack measurements in (a) 15-m interval; (b) 30-m interval.

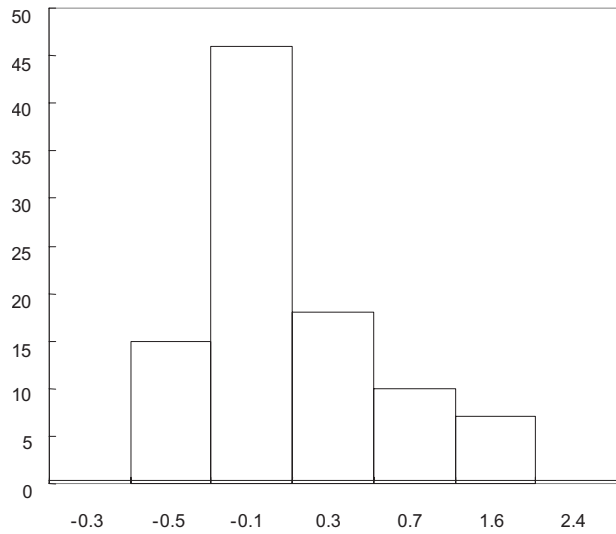


FIG. 11—Histogram of ϵ ($\Delta L_r = 15$ m).

measurements with the Crackscope were conducted in three different runs.

Figure 9(a) presents the stitched images of a 15-m (roughly 50-ft) section scanned by the Crackscope at a speed of 55 km/h, and Fig. 9(b) and 9(c) displays the corresponding crackmaps drawn by an expert and the Crackscope. The length and orientation of cracks in the manual crackmap were estimated and depicted on 0.6×0.6 m² (2×2 ft²) grids while the expert walked on the pavement. The crackmap generated by the Crackscope showed the detected cracks that were counted in the measurements. Except differences in some details, the two crackmaps did coincide, demonstrating the automatically generated crackmap from the Crackscope provides a reasonably good representation of crack locations.

The data accuracy of the Crackscope was evaluated by comparing the Crackscope data with the manual measurements in a certain distance interval. The manual and Crackscope data were first aligned at the same starting point, and then summed up in separate intervals, such as 15, 30, 60,..., 480 m (approximately 50, 100, 200,..., 1600 ft). Since in the manual measurement crack types, e.g., transverse, longitudinal, or alligator, were not differentiated, the crack data included only the total length of the cracks in an interval. Figure 10(a) and 10(b) show the crack lengths of this pavement section plotted in 15- and 30-m distance intervals. Overall, the Crackscope measurements summed in both intervals exhibit a high consistency in three different runs, and show similar trends as the manual measurements, but the variations in the 15-m interval

TABLE 1—System errors in different intervals.

Interval ΔL_r (m)	15	30	60	120	240
Crack length \bar{L}^v (m)	26.64	53.28	106.55	213.11	426.21
ϵ Mean $\bar{\epsilon}$	0.15	0.12	0.10	0.09	0.06
Standard deviation S_ϵ	0.55	0.47	0.37	0.30	0.29
E Mean \bar{E}	0.31	0.36	0.39	0.39	0.34
Standard deviation S_E	1.49	1.64	1.61	1.56	1.76

TABLE 2— χ^2 test statistic data of E .

i	Bin Interval	f_i	\hat{p}_i	$n\hat{p}_i$	$f_i - n\hat{p}_i$	$(f_i - n\hat{p}_i)^2 / n\hat{p}_i$
1	$(-\infty, -1.21)$	12	0.15	14.63	-2.63	0.47
2	$[-1.21, -0.21)$	24	0.21	20.11	3.89	0.75
3	$[-0.21, 0.79)$	29	0.26	25.29	3.71	0.55
4	$[0.79, 1.79)$	17	0.21	20.56	-3.56	0.62
5	$[1.79, 2.79)$	6	0.11	10.81	-4.81	2.14
6	$[2.79, +\infty)$	8	0.05	4.60	3.40	2.50
$\chi^2 = \sum_{i=1}^6 (f_i - n\hat{p}_i)^2 / n\hat{p}_i$						7.03

are noticeably higher than those in the 30-m interval. Since crack data vary with the selected distance intervals, it is necessary to investigate how the system accuracy changes with the intervals.

For a given pavement section L_r , the crack lengths resulted from the automated and manual methods are denoted as L^a and L^v , respectively. If the section is divided equally into m subsections to report m crack data and the automated surveys are repeated n times, the each subsection length, that is, distance interval, is $\Delta L_r = L_r / m$, and the crack lengths measured visually (expert) and automatically (Crackscope) in the i th sub-section are denoted as L_i^v and L_{ij}^a ($i = 1, 2, \dots, m$, $j = 1, 2, \dots, n$). If the expert's data are taken as true measurements, the error ε_{ij} of the Crackscope measurements in the i th subsection and j th run can be defined as

$$\varepsilon_{ij} = \Delta L_{ij} / L_i^v = (L_{ij}^a - L_i^v) / L_i^v. \quad (10)$$

Figure 11 displays the histogram of ε when $\Delta L_r = 15$ m. The distribution of ε appears to be normal, and the ε sample mean $\bar{\varepsilon}$ and standard deviation S_ε in different ΔL_r are listed in Table 1. These data indicate that $\bar{\varepsilon}$ and S_ε decreased with the selected distance interval, i.e., the crack length \bar{L}^v . The larger the interval, the longer the summed crack length, and the smaller the mean error $\bar{\varepsilon}$ and error variability S_ε . Although this trend is reasonable, ε cannot be directly used to estimate the accuracy because it varies with the crack measurement L^v . We constructed another error statistic, E , which is almost invariant to the crack measurements or the intervals as follows:

$$E = \ln(L^v) \frac{\Delta L}{L^v} = \ln(L^v) \varepsilon \quad (11)$$

The means (\bar{E}) and the standard deviations (S_E) of E in different ΔL_r s are also listed in Table 1. It can be seen that the changes in \bar{E} and S_E remain in small ranges and exhibit no apparent trends.

Pearson's chi-square (χ^2) method was applied to the random variable E to test the goodness of fit to a normal distribution. We have a hypothesis $H_0: E \sim N(\mu, \sigma^2)$. The χ^2 test statistical data are listed in Table 2 for $\Delta L_r = 15$ m. The number (k) of bins is set to be 6 when the sample size is 96 for $\Delta L_r = 15$ m. In the Table 2, i is the order number of the bins, the second column lists the interval of the corresponding bin, f_i , \hat{p}_i , and $n\hat{p}_i$ are the observed frequency, expected probability, and expected frequency for the i th bin, respectively. The test statistic $\chi^2 = \sum_{i=1}^k (f_i - n\hat{p}_i)^2 / n\hat{p}_i$ approximately follows a χ^2 distribution with $k - r - 1$ degree of freedom, where r is the number of the parameters of the expected distribution (for a normal distribution, $r = 2$). Thus, the degree of freedom is 3. If the significance level $\alpha = 0.01$, H_0 can be accepted because

$$\chi^2 = 7.03 < \chi_{\alpha}^2(k - r - 1) = \chi_{0.01}^2(3) = 11.345 \quad (12)$$

where:

$\chi_{\alpha}^2(k - r - 1) = \chi^2$ distribution critical value with $k - r - 1$ degree of freedom and at α level of significance.

When H_0 is accepted, the parameters μ and σ can be determined using the average of the sample mean \bar{E} and standard deviation S_E at $\Delta L_r = 15$ m. Therefore, we get

$$E \sim N(\mu, \sigma^2), \quad \mu \approx 0.311, \quad \sigma \approx 1.487 \quad (13)$$

The manual measurement L^v is often unknown. The crack length L' resulted from the automated measurement can be used to estimate the error mean $\bar{\varepsilon}$

$$\bar{\varepsilon} = \mu / \ln(L') \quad (14)$$

Given a confidence level $(1 - \alpha)$, the confidence interval (lower ε_{low} and upper ε_{up} limits) of the $\bar{\varepsilon}$ also can be calculated:

$$\varepsilon \in (\varepsilon_{\text{low}} | \alpha, \varepsilon_{\text{up}} | \alpha) = \left(\frac{\mu - u_{\alpha/2} \sigma}{\ln(L')}, \frac{\mu + u_{\alpha/2} \sigma}{\ln(L')} \right) \quad (15)$$

where:

$u_{\alpha/2}$ = right off point with $\alpha/2$ in the normal distribution.

Figure 12 shows the estimated errors at various given crack lengths, and the curves of the corresponding confidence intervals at confidence level $1 - \alpha = 0.90$, which were calculated from Eqs 14 and 15. In Fig. 12, the x and y axes represent the measured crack length, the corresponding error and the upper and lower bounds of the error at different confidence levels. In general, the error $\bar{\varepsilon}$ of the Crackscope system is lower than 10 % for the measured crack lengths, and the error confidence interval becomes smaller when the summed crack length, or distance interval, gets larger.

The repeatability of the Crackscope was evaluated with the cracking data collected in multiple runs on the selected pavement. If D_{ikl}^a denotes the difference in crack lengths between the k th and l th runs in the i th subsection, it can be calculated as follows:

$$D_{ikl}^a = L_{ik}^a - L_{il}^a, \quad k \neq l \quad (16)$$

where:

$k, l = 1, 2, 3$ in our experiment.

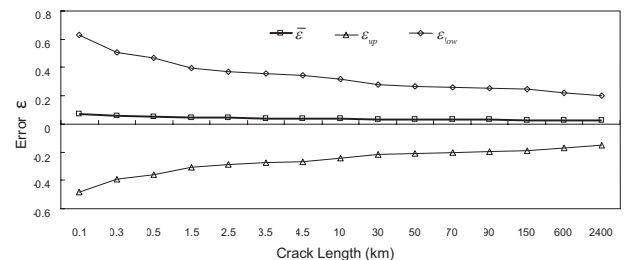
FIG. 12— ε and crack length.

TABLE 3— χ^2 test statistic data of D_{ikl}^a

i	Bin Interval	f_i	\hat{p}_i	$n\hat{p}_i$	$f_i - n\hat{p}_i$	$(f_i - n\hat{p}_i)^2 / n\hat{p}_i$
1	$(-\infty, -9.81)$	5	0.05	4.86	0.14	0.00
2	$[-9.81, -4.41)$	12	0.19	17.83	-5.83	1.91
3	$[-4.41, 1.00)$	44	0.34	33.02	10.98	3.65
4	$[1.00, 6.40)$	23	0.29	27.75	-4.75	0.81
5	$[6.40, +\infty)$	12	0.13	12.54	-0.54	0.02
$\chi^2 = \sum_{i=1}^5 (f_i - n\hat{p}_i)^2 / n\hat{p}_i$						6.40

D_{ikl}^a are sampling values of a random variable D^a . The χ^2 test was used to verify the normality of D^a . The null hypothesis: $H_0: D^a \sim N(\mu, \sigma^2)$. Table 3 lists the χ^2 test statistic data. It was found that H_0 can be accepted at a confidence level of $1 - \alpha = 0.99$ because $\chi^2 = 6.40 < \chi_{\alpha}^2(k - r - 1) = \chi_{0.01}^2(2) = 9.210$.

The analysis of variance (ANOVA) method was applied to examine the identity of the means of D_{i12}^a , D_{i23}^a , and D_{i31}^a , and the hypothesis, H_0 , is D_{i12}^a , D_{i23}^a , and D_{i31}^a were drawn from the same normal population D^a . Table 4 shows the mean and variance of the differences in crack length between different runs when the cracking data was collected in a distance interval of 15 m. The mean difference between any two of these three runs are relatively small.

Table 5 presents the ANOVA results, where SS, df, and MS are the sum of square (of deviation), degree of freedom, mean of sums of square, respectively. F is the test statistic, and F_c is the critical value of the F distribution with two degrees of between-groups and 93 degrees of within-groups at the significant level of 0.05. P indicates the probability of obtaining a test statistic at least no less than the one that actually observed. The higher the P , the more significant the identity between the groups. Because $P > \alpha = 0.05$ and $F = 0.0094 < F_{0.05}(2, 93) = 3.094$, the hypothesis, H_0 , can be accepted. Based on the two verified hypotheses, it can be concluded that the difference in crack length measurements between any two runs is insignificant, and therefore the system shows a good repeatability.

Summary

A line-scan GigE camera and a laser line projector can provide a reliable and high-speed image acquisition method for pavement cracking inspection. The laser projector provides sufficient illumination for the camera to capture analyzable images in both daytime and nighttime, and effectively eliminates sunlight shadows when a suitable band-pass filter is used. The proximity sensor and speed modulation can automatically shut off the laser while the vehicle stops or in a slow motion to avoid possible harm to human eyes. The customized crack detection software mainly consists of seed detec-

TABLE 4—Difference in crack length among different runs.

Groups	Count	Mean	Variance
D_{i12}^a	32	-0.11	30.85
D_{i13}^a	32	-0.15	57.08
D_{i32}^a	32	0.04	17.66

TABLE 5—ANOVA.

Source of Variation	SS	df	MS	F	P	F_c
Between groups	0.66	2	0.33	0.0094	0.99	3.09
Within groups	3273.47	93	35.20			

tion and connection algorithms. The experiments on a designated pavement showed that the difference in crack length between the manual and automatic measurements was less than 10 %, and no significant difference among the multiple scans by the system.

Acknowledgements

This research project was sponsored by Texas Department of Transportation from 2006 to 2008. We are grateful for the manual pavement data provided by the project director, Todd Copenhagen, at TxDOT.

References

- [1] Mendelsohn, D. H., "Automated Pavement Crack Detection: An Assessment of Leading Technologies," *Proc., 2nd North Am. Conf. on Managing Pavements*, Vol. 3, Toronto, Nov. 2–6, Ministry of Transportation, Ontario, Canada, FHWA and U.S. Department of Transportation, Washington, D.C., 1987, pp. 3.297–2.314.
- [2] Saraf, C. L., 1998, "Pavement Condition Rating System, Review of PCR Methodology," *FHWA-OH-99-004*, FHWA, U.S. Department of Transportation, Washington, D.C.
- [3] Cheng, H. D., Jiang, X., Li, J., and Glazier, C., "Automated Real-Time Pavement Distress Analysis," *Transp. Res. Rec.*, Vol. 1655, 1999, pp. 55–64.
- [4] Wang, K. C., "Automated System for Pavement Surface Distress Survey: A Historical Perspective on Design and Implementation," *Proc. Transport Research Board 77th Annual Meeting*, Jan. 12–13, Transportation Research Board, Washington, D.C., 1998.
- [5] Wang, K. C., "Use of Digital Cameras for Pavement Surface Distress Survey," *Trans. Res. Rec.*, Vol. 1675, 1999, pp. 91–97.
- [6] Zhou, J., Huang, P. S., and Chiang, F. P., "Wavelet-Based Pavement Distress Detection and Evaluation," *Opt. Eng.*, Vol. 45(2), 2006, p. 027007.
- [7] WayLink Systems Co., Automated Distress Analyzer, 2007, <http://www.waylink.com> (Last accessed January 2011).
- [8] Roadware Group Inc., Automated Road Analyzer, 2011, <http://www.roadware.com> (Last accessed January 2011).
- [9] International Cybernetics Co., Imaging vehicle and software, 2010, http://www.intlcybernetics.com/imaging_products.htm (Last accessed January 2011).
- [10] CSIRO Australia Roads and Traffic Authority, Road Crack Detection, 2007, <http://www.cmis.csiro.au/iap/RecentProjects/roadcrack.htm> (Last accessed January 2011).
- [11] Xu, B., "Summary of Implementation of an Artificial Light System for Automated Visual Distress Rating System," *Tech-*

- nical Report No. 5-4958-01-1, Center for Transportation Research, The University of Texas at Austin, Austin, TX, August 2008, http://www.utexas.edu/research/ctr/pdf_reports/5_4958_01_1.pdf (Last accessed January 2011).
- [12] INO Canada, Laser Road Imaging System, 2008, <http://www.ino.ca/enca/achievements/description/project-p/laser-road-imaging.html> (Last accessed January 2011).
- [13] Xu, B., Yao, X., and Yao, M., "Design of CrackScope (VCrack)," *Technical Report No. 0-5708-1*, Center for Transportation Research, The University of Texas at Austin, Austin, TX, October 2007, http://www.utexas.edu/research/ctr/pdf_reports/0_5708_1.pdf (Last accessed January 2011).
- [14] Xu, B. and Huang, Y., "Real-Time, Automated Surface Distress Measurement System," U.S. Patent No. 7697727 (Apr. 13, 2010).
- [15] McGhee, K. H., "Automated Pavement Distress Collection Techniques, a Synthesis of Highway Practice," *NCHRP Synthesis 334*, Transportation Research Board of the National Academies, Washington, D.C., 2004.
- [16] Howe, R. and CleMena, G. G., *An Assessment of The Feasibility of Developing and Implementing an Automated Pavement Distress Survey System Incorporating Digital Image Processing*, Virginia Transportation Research Council, Richmond, VA, 1997, p. 78.
- [17] Wang, K. C. P., 2003, "Automated Imaging Technologies for Pavement Distress Survey," *Transportation Research Circular*, Committee A2B06, Transportation Research Board, National Research Council, Washington, D.C.
- [18] Cheng, H. D., Chen, J.-R., Glazier, C., and Hu, Y. G., "Novel Approach to Pavement Cracking Detection Based on Fuzzy Set Theory," *J. Comput. Civ. Eng.*, Vol. 13(4), 1999, pp. 270–280.
- [19] Cheng, H. D., Wang, J. L., Hu, Y. G., Glazier, C., Shi, X. J., Chen, X. W., "Novel Approach to Pavement Cracking Detection Based on Neural Network." *Transp. Res. Rec.*, Vol. 1764, 2001, pp. 119–127.
- [20] Koutsopoulos, H. N., El Sanhoury, I., and Downey, A. B., "Analysis of Segmentation Algorithms for Pavement Distress Images," *J. Transp. Eng.*, Vol. 119(6), 1993, pp. 868–888.
- [21] Li, L., Chan, P., Rao, A., Lytton, R. L., "Flexible Pavement Distress Evaluation Using Image Analysis," *Proceedings of the 2nd International Conference on Applications of Advanced Technologies in Transportation Engineering*, Minneapolis, MN, Aug. 18–21, ASCE, New York, 1991.
- [22] Wang, K. C. P., Li, Q., and Gong, W., "Wavelet-Based Pavement Distress Image Edge Detection with a Troun Algorithm," *Transp. Res. Rec.*, Vol. 2024, 2008, pp. 73–81.
- [23] Huang, Y. and Xu, B., "Automatic Inspection of Pavement Cracking Distress," *J. Electron. Imaging*, Vol. 15(1), 2006, pp. 013017.